東北大学機関リポジトリ
TOUR
Tohoku University Repository

Isothermal γ → ε phase transformation behavior in a Co-Cr-Mo alloy depending on thermal history during electron beam powder-bed additive manufacturing

著者	Yufan Zhao, Yuichiro Koizumi, Kenta Aoyagi, Kenta Yamanaka, Akihiko Chiba
journal or publication title	Journal of Materials Science & Technology
volume	50
page range	162-170
year	2020-08-01
URL	http://hdl.handle.net/10097/00135603

doi: 10.1016/j.jmst.2019.11.040

Creative Commons : 表示 - 非営利 - 改変禁止
http://creativecommons.org/licenses/by-nc-nd/3.0/deed.ja

Research Article

Isothermal γ → ε phase transformation behavior in a Co-Cr-Mo alloy depending on thermal history during electron beam powder-bed additive manufacturing

Yufan Zhao [1], Yuichiro Koizumi [2, a], Kenta Aoyagi [2, *], Kenta Yamanaka [2], Akihiko Chiba [2]

[1] *Department of Materials Processing, Graduate School of Engineering, Tohoku University, 6-6-11 Aoba, Aramaki, Aoba-ku, Sendai 980-8579, Japan*

[2] *Institute for Materials Research, Tohoku University, 2-1-1 Katahira, Aoba-ku, Sendai 980-8577, Japan*

* Corresponding author. Ph.D.; Tel.: +81 022 2152118.

E-mail address: k.aoyagi@imr.tohoku.ac.jp (K. Aoyagi).

a *Present address: Division of Materials and Manufacturing Science, Graduate School of Engineering, Osaka University, 2-1, Yamadaoka, Suita, Osaka 565-0871, Japan*

Powder bed fusion with electron beam (PBF-EB), allows Co-Cr-Mo (CCM) implants with patient-customization to be fabricated with high quality and complex geometry. However, the variability in the properties of PBF-EB-built CCM alloy, mainly due to the lack of understanding of the mechanisms that govern microstructural heterogeneity, brings limitations in extensive application. In this study, we characterized the microstructural heterogeneity regarding the γ-fcc → ε-hcp phase transformation. The phase transformation during PBF-EB was analyzed depending on the thermal history that was elucidated by the numerical simulation. It revealed that isothermal γ → ε transformation occurred during the fabrication. Importantly, the difference in γ/ε phase distribution was a result of the thermal history determining which method phase transformation was taking place, which can be influenced by the PBF-EB process parameters. In the sample with a low energy input (E_{area}= 2.6 J/mm^2), the martensitic transformation was dominant. As the building height increased from the bottom, the ε phase fraction decreased. On the other hand, in the sample with a higher energy input (E_{area}= 4.4 J/mm^2), the ε phase formed via diffusional-massive transformation and only appeared in a short range of the lower part away from the bottom.

Keywords: Powder bed fusion with electron beam; Phase transformation; Thermal history; Numerical simulation

1. Introduction

CoCr-based alloys are the proper choice of medical biomaterials. Especially the CoCrMo (CCM) alloy, which does not contain the element nickel that can induce allergy or even cancer, can be applied to the bone implants owing to the excellent mechanical properties and corrosion resistance [1].

Additive manufacturing (AM), assisted by the computer-aided design, has played an essential part in the development of aerospace components, automotive and energy application parts, and medical implants [2]. Powder bed fusion with electron beam (PBF-EB) is an AM system that utilizes a high-energy electron beam to melt metal powders and fabricates full-dense metallic parts in a layer-building fashion [3]. The heat source and working chamber atmosphere (about 0.1 Pa) are different from those of the selective laser melting process, which is in favor of PBF-EB to be beneficial for materials that contain active elements. PBF-EB has successfully produced many bone implants such as the knee, hip-joint, and jaw [4], and permits CCM bone implants with patient-customization to be produced and to possess high forming quality and complex geometry [5][6].

The investigations on the microstructure of PBF-EB-built CCM alloys have attracted researchers' interests. X. P. Tan et al. studied the microstructure characteristics and the role of carbide in determining the mechanical properties [7][8]. D. D. Xiang et al. investigated the anisotropy in microstructure and the correlated mechanical properties [9]. Notably, it was reported that the microstructural variations of phase constitutions could be caused by a cyclical heating and melting of the successive layer-by-layer AM deposition process [10]. The resultant thermal history determines the phase transfer sequence and the final as-built microstructure, for example, the distribution of α/β phases in Ti-6Al-4V [11][12]. Likewise, in terms of the matrix phase constitution in additively manufactured CCM alloy, the microstructural heterogeneity may present along the building direction. There are two equilibrium phases in CCM alloys — one is γ-face-centered cubic (fcc) phase, which is stable at high temperature, typically exceeding 900 °C; the other is ε-hexagonal closed packed (hcp) phase which is stable at a lower temperature. In PBF-EB, after the far-from-equilibrium solidification immediately, the γ-fcc phase can exist as a metastable phase even at a low temperature where the ε-

hcp phase is stable. However, the repeated heating at a temperature of 1123 K and subsequent thermal cycling facilitate the phase constitution to vary spatially. According to the studies conducted by Sun et al. [13] and Wei et al. [14], along the building direction of the as-built sample, the constituent phase varied from single ε-hcp phase in the bottom to single γ-fcc phase in the top. The repeated heating process that acts as an aging process promotes the isothermal phase transformation from the metastable γ-fcc phase to the stable ε-hcp phase in the early-built parts. Takashima et al. [15] investigated the effect of relative building position in the horizontal plane of a base plate on phase distribution in PBF-EB-built CCM alloy. They found that the difference in the relative building position generated different γ/ε phase fractions, because of the difference in thermal history.

Microstructural heterogeneity (i.e., the distributions and fractions of γ-fcc and ε-hcp phases) significantly affects the mechanical properties of PBF-EB-built CCM alloy, since the phase transformation from γ-fcc to ε-hcp enhances the wear-resistance but deteriorates the ductility of the component [16]. Manipulation of the phase constitution is essential to obtain the required performance of PBF-EB-built CCM alloy. Depending on the thermal history, the isothermal γ-fcc → ε-hcp phase transformation in CCM alloy can take place via diffusional-massive transformation or diffusionless-martensitic transformation whose characterizations, theories and models have been in general established and known according to numbers of literature [17][18][19][20]. Alloys undergoing massive transformations whose driving force is the difference in free energy, will generally also transform in a martensitic manner when they are aged at a low aging temperature (isothermal-martensitic) to overwhelm the nucleation of the massive ε phase [19]. Though prior studies [13][14][15][21][22] revealed the variability of critical microstructural features of AM-built CCM alloy, the more in-depth understanding of the phase transformation behaviors that govern microstructural heterogeneity and expected flexible control still deserve much of exploration.

Concerning the alloys that undergo phase transformations, the effect of thermal history on resultant microstructure must be considered. For evaluating the thermal field of the sample during AM fabrication, numerical modeling techniques have emerged to help researchers predicting the thermal history in laser aided AM [23][24] and electron beam aided AM [25][26]. In this study, the microstructural heterogeneity in terms of matrix phase constitution of PBF-EB-built Co-28Cr-6Mo alloy was characterized. The present paper addressed the effect of the thermal history during the PBF-EB process on the isothermal γ→ ε phase transformation, aided by the numerical simulation of thermal history evaluation.

2. Methodology

2.1 PBF-EB processing and microstructure characterization

The samples with cube-shape and dimensions of 10 mm ×10 mm ×10 mm were produced using an Arcam®A2X machine. A gas-atomized Co-28Cr-6Mo alloy powder (mean diameter: 65 μm) was applied under a layer thickness of 70 μm. Table 1 shows the composition of the alloy powder measured by ICP-AES. The electron beam power (P) ranged between 100 and 1000 W, and the scan speed (V) ranged between 100 and 10000 mm/s. The process parameters in Fig. 1 were determined depending on our prior experience of processability for CCM. For ensuring the dense formations, the pre-implemented single-track melting experiments determined the line offset (l_{off}) according to the dimensions of the melt region. Under such line offsets, the overlap between the adjacent melt tracks should be more than 1.5 times of the layer thickness. The resulting line energy ($E_{\mathrm{line}} = P/V$) ranged between 0.1 and 10 J/mm, and the area energy ($E_{\mathrm{area}} = P/(V \cdot l_{\mathrm{off}})$) ranged between 2.2 and 11 J/mm^2. The preheating temperature was kept at 1123 K for all of the samples to avoid powder smoke. A *xy*-scanning strategy in which the bidirectional scanning direction was rotated by 90° in each layer was applied for the building process.

The block samples were cut along the building direction (z-axis) using a wire electric discharge machine. The sectioned samples were ground and polished by standard metallographic techniques followed by a final polishing using 0.04 μm colloidal silica suspension for one hour. Electron backscattered diffraction (EBSD) and scanning electron microscopy based on the backscattered electron (BSE) signals were then utilized to analyze the microstructure near the center of the width in each sample. By characterizing the numbers of samples in this working session, the research of grain morphology and texture formation under systematically varied process conditions was performed at first [27]. Afterwards, the phase transformation behaviors depending on the thermal history will be discussed in the present study.

2.2 Numerical simulation for evaluating thermal history

We have established a 3D heat transfer model that developed using a commercial Multiphysics-modeling program—Flow 3D® [28]. The energy efficiency of the electron beam was assumed to be 90% [29]. The heat loss of the object was induced by conduction and radiation. Given the vacuum condition (about 0.1 Pa) in the PBF-EB building chamber, cooling by air convection was neglected,

which also improved the calculation efficiency. Our previous study [30] described the thermophysical properties of the material, parameters/coefficients applied in the simulation, and modeling validation.

To ensure reasonable calculation accuracy yet affordable time expense of simulation, we performed a 3D steady-state heat transfer simulation with some simplifications. As with rapid electron beam translation speed (~ 10000 mm/s) in this work, the moving-spot heat source was approximated as an equivalent plane heat source P_{plane}, shown in Fig. 2(a). In addition, since the layer thickness (70 μm) was much smaller than the height of the samples (10000 μm), the layer-by-layer building was simplified as bulk increment with each increment height of 2500 μm (Fig. 2(b)). While building the samples, the heat source was carried out in a loop: $\Delta t_{\text{scan}} \times n_1$ ($P_{\text{plane}} = P_{\text{spot}}$) → $\Delta t_{\text{standby}}$ ($P_{\text{plane}} = 0$), repeating as n_2 times. Δt_{scan} was the duration for a single-track scan, and n_1 was the scan numbers of one layer in a sample. $\Delta t_{\text{standby}}$ was the duration for the building of all the other samples in one-layer except the targeted sample, and n_2 was the effective layer number of a bulk increment.

3. Results

3.1 Isothermal γ → ε phase transformation during PBF-EB

As described in Section 1, during PBF-EB, the earlier built part is kept at high temperatures during the subsequently repeated melting process that is similar to an isothermal-aging treatment. Thus, the γ → ε phase transformation can occur at the lower part of a PBF-EB-built CCM alloy with considerable height.

Figure 3 shows the EBSD phase map of vertical cross-sectional microstructure and EBSD pole figures of selected ε grain and original γ grain at the lower part of an as-PBF-EB-built sample. On the left side of Fig. 3(a), the ε grain grew across the grain boundary of the adjacent γ grain. There was no S-N OR between the ε grain and the adjacent γ grain (Fig. 3(b)), which indicated that the ε phase here formed due to isothermal aging involving a diffusional-massive transformation. On the other hand, on the right side of Fig. 3(a), the ε grains were embedded within the original γ grain. The corresponding EBSD pole figures (Fig. 3(c)) revealed that the Shoji-Nishiyama orientation relationship (S-N OR: $(111)_\gamma \,//\, (0001)_\varepsilon$; $[10\bar{1}]_\gamma // [11\bar{2}0]_\varepsilon$) was satisfied between the new ε grain and the original γ grain. Figure 3(c) indicated that the ε phase observed here originated from

the isothermal γ → ε martensitic transformation in which the nucleation and growth of new ε grain are limited within the original γ grain. The above results suggested that the isothermal γ → ε phase transformation taken place via both diffusionless-martensitic and diffusion-massive manners in the as-PBF-EB-built sample. These two different manners are thought to be competitive with each other, depending on the temperature condition [19][31].

3.2 Distributions of γ and ε phases in as-PBF-EB-built samples

Since the relative position of the sample on the base plate affects the conditions of heat accumulation and conduction [15], the samples located at axisymmetric positions with respect to the base plate were selected for observation. Moreover, among the numbers of building samples, there were two kinds of typical microstructure in terms of the ε phase distribution region along the building height. The selected two samples (Sample A and Sample B) located at axisymmetric positions with respect to the base plate, exactly exhibited these two typical microstructural features regarding the distributions of γ and ε phases. In Fig. 4(a), Sample A and Sample B under different process parameters and located on both sides of the base plate, were taken as the subjects of the study. Fig. 4(c)(d) show the EBSD IPF maps and phase maps of cross-sectional microstructures in different parts along the building height. The orientation shown in the IPF maps was in the normal direction (*x*-direction in Fig. 4(b)). γ and ε phases in the phase maps were colored as red and green, respectively. In Sample A (Fig. 4(c)), the fraction of the ε phase decreased from the bottom to the top of the sample. Notably, being different from the results of Sample A and previous studies [13][14][15][21][22], in Sample B (Fig. 4(d)), there was no ε phase in the top and bottom but ε phase appeared only in a short range of the lower part away from the bottom. As with the similar conditions of heat accumulation and conduction, the difference in ε phase distribution between Sample A and Sample B was considered to originate from the variation of thermal history influenced by the process parameters under the given sample size/geometry and the corresponding building period.

3.3 Thermal history during PBF-EB

Figure 5 shows the experimental thermal history during the PBF-EB process at the bottom center of the base plate measured by a thermocouple equipped in the building chamber. The maintained temperature range during the building period was in accordance with that of a study on CCM alloy building conducted by our group previously [32]. The variation in temperature corresponded to the

process stages consisting of (i) preheating process in which the base plate is heated to the pre-set temperature (1123 K) by using a de-focused beam at a considerably high scan speed of 14600 mm/s; (ii) heating & building process in which preheating repeats following the building of each layer to slightly sinter the newly raked powder and keep the temperature of the base plate to be almost constant; and (iii) cooling after completion of the total build objects. As can be seen, until the electron beam turned off, the efficient building process went on for about 4 hours.

Before the start of the building process, the base plate has been heated to the presetting high temperature that is the necessary initial condition of temperature field for subsequent sample forming. The simulated temperature field of the base plate is shown in Fig. 6. The base plate was heated by an equivalent plane heat source with a power of 2280 W (standard parameter of heating) till the temperature in the bottom center reached 1098 K (the average temperature during the heating & building process (Fig. 5)). Though the bottom center reached the temperature of 1123 K, the upper surface of the base plate presented lower temperature and possessed a reducing trend from the center to the edge because of heat conduction and dissipation. Then the temperature field of the base plate acted as the thermal boundary condition for simulating the thermal history of each sample. Figure 7 showed the simulated temperature evolutions of Sample A and Sample B. When the samples began to be built on the plate, the local thermal conduction inevitably increased so that the base plate temperature further reduced reasonably to be lower than the initial temperature of 996 K (Fig. 6). Note that, as build height increased (from increment ① to ④), the temperature of the center position in each increment increased because the building region was becoming far from the base plate accompanied with reduced thermal conduction but increased thermal accumulation, which was a result of the long distance for the heat transfer through the earlier-built part. Besides, as with more considerable energy input ($E_{\text{area}} = 4.4$ J/mm^2) of Sample B than that ($E_{\text{area}} = 2.6$ J/mm^2) of Sample A, the individual increment in Sample B possessed a higher temperature than the corresponding increment in Sample A.

4. Discussion

4.1 The effect of thermal history on the isothermal γ → ε phase transformation method

The isothermal martensitic transformation occurs at 973 K or below, while the massive transformation is dominant at a higher temperature range [19]. The diffusional-massive

transformation occurs via a short-range diffusion process and associated interface migration, involving a kinetic process [33][34]. The solid-state transformation usually involves nucleation and growth and is generally described by the Johnson–Mehl–Avrami–Kolmogorov (JMAK) model in which nucleation and growth rates are time-dependent under isothermal condition [35]. The phase transition rate (X) is a function of holding time (t):

$$X = 1 - \exp(-kt^n), \quad (1)$$

where k is the coefficient of the temperature-dependent reaction rate, and n is a constant dependent on the nature of growth mechanisms involved in the transformation (Avrami). For the case of nuclei with the number of n_0 per unit volume appearing at the same, $k = (4\pi/3)n_0 r_\varepsilon^3$ [36]. Then

$$X(\gamma \rightarrow \varepsilon) \approx 1 - \exp\{-(4\pi/3)n_0 r_\varepsilon^3 t^3\}, \quad (2)$$

where n_0 is the nuclei density (m^{-3}). The growth rate of the ε phase r_ε is expressed as

$$r_\varepsilon = \left(D_{Co}^{\gamma/\varepsilon}/\delta RT\right) \cdot \Delta G_{\gamma\rightarrow\varepsilon}, \quad (3)$$

where $D_{Co}^{\gamma/\varepsilon}$ is the diffusion coefficient of cobalt ($m^2 \cdot s^{-1}$) obtained in [37], $\Delta G_{\gamma\rightarrow\varepsilon}$ is the difference in free energy between γ and ε phases ($J \cdot mol^{-1}$) calculated by Thermo-Calc [38], and δ is the γ/ε interface width of three atomic sites (4.5×10^{-10} m) [39]. From the above calculation, the isothermal TTT curve of the γ → ε diffusional-massive transformation was obtained and shown in Fig. 8. The left curve with red and the right curve with green represented the start and the end (ε phase volume fraction of 100 %) of the transformation, respectively. This diagram showed a good agreement with the experimental data in [19]. The temperature region for martensitic transformation should locate below this TTT curve.

From the simulated temperature fields of each part shown in Section 3.3 (Fig. 7), the temperature ranges that Sample A and Sample B underwent during PBF-EB are annotated on the right side of Fig. 8. Accordingly, the middle and lower parts of Sample A were roughly at the temperature range of martensitic transformation. On the other hand, as with more considerable energy input ($E_{\text{area}} = 4.4$ J/mm^2) of Sample B than that ($E_{\text{area}} = 2.6$ J/mm^2) of Sample A, Sample B was generally kept at a higher temperature range of massive transformation. EBSD data can help to clarify which method the γ → ε phase transformation is taking place. Figure 9 shows the pole figures taken from the γ and ε phases in the middle and lower parts of Sample A and Sample B. S-N OR: $(111)_\gamma // (0001)_\varepsilon$; $[10\bar{1}]_\gamma // [11\bar{2}0]_\varepsilon$ between γ and ε phases was observed in Sample A, while no clear orientation correlation between γ and ε phases was observed in Sample B. In addition, the histograms of the

misorientation angle between adjacent ε phase in Sample A and Sample B are shown in Fig. 10. In the case of martensitic transformation, the four martensite variants corresponding to the $(0001)_\varepsilon$ plane transformed from the four $\{111\}_\gamma$ planes would present the expected misorientation angle of 70.5° [40]. Hence, in Sample A (Fig. 10(a)), there was a peak near 70.5° in the histogram of the misorientation angle, which clearly showed that the martensitic transformation with S-N OR was dominant. In sample B (Fig. 10(b)), no apparent peak near 70.5° was recognized, indicating that the ε phase with near-random orientation formed here via diffusional-massive transformation. The above results showed a good agreement between the simulated temperature fields and phase transformation behaviors clarified by experiments. We can conclude that under a given sample size/geometry and the corresponding building period, the process parameters influence the thermal history, and subsequently, the γ → ε phase transformation behaviors in CCM alloy during PBF-EB.

4.2 The effect of thermal history on the distributions of the ε phase

As with the similar conditions of heat accumulation and conduction correlated to the relative positions on the base plate, the difference in γ/ε phase distributions between Sample A and Sample B should be closely related to the thermal history.

The building period of PBF-EB based on experimental temperature history beneath the center of the base plate (Fig. 5), is additionally annotated in Fig. 8. In Sample A, the temperatures of the middle and lower parts were estimated in the range of martensitic transformation, as discussed in the above section. The kinetics of isothermal martensitic transformation is difficult to evaluate without a specific experiment because the rate controlling mechanisms are sophisticated and do not yield general rules [41][42]. Nevertheless, the displacive-martensitic transformation is coordinated action rather than a diffusional movement. Thus, the propagation of ε-martensite is assumed not to show significant time dependency as massive transformation possesses [43]. As the building height increased far and far from the base plate, the holding time for isothermal γ → ε martensitic transformation decreased. Though the top of Sample A was held at the temperature range for massive transformation, the holding time was too short for the transformation taking place (Fig. 8). Accordingly, the ε phase fraction decreased with increasing distance from the bottom of Sample A (Fig. 4(c)) in which isothermal γ → ε martensitic transformation was dominant during PBF-EB.

Sample B experienced a temperature history in the range of massive γ → ε transformation or higher, as with more considerable energy input ($E_{\text{area}} = 4.4$ J/mm^2) of Sample B than that ($E_{\text{area}} =$

2.6 J/mm^2) of Sample A. We can see from Fig. 8, in the upper part, the temperature achieved was almost higher than that of the γ → ε transition range, and thus, single γ phase was inferred to remain without phase transformation after the completion of PBF-EB building process. The lower part was mainly kept at the range for massive transformation. Notably, as the position was getting closer to the bottom (from increment ② to ① of Sample B in Fig. 8), the period required for activation of massive γ → ε transformation increased and even became longer than the total period of heating & building during PBF-EB. Thus, no ε phase appeared in the lowest part of Sample B, even though the part underwent the longest holding time. Above can explain why the ε phase presented only in a short range of the lower part away from the bottom of Sample B (Fig. 4(d)) where the period required for massive γ → ε transformation is relatively short (Fig. 8). The results also indicated that the martensitic transformation carried out more easily and quickly than massive transformation during the isothermal aging process of post-melting in PBF-EB.

The above discussion suggests that the difference in γ/ε phase distribution is a result of the thermal history determining the method by which the γ→ ε phase transformation is taking place. Accordingly, the phase transformation can be controlled by manipulating the process parameters under a given sample size/geometry and the corresponding building period. For example, in Fig. 11, the sample almost without the ε phase was fabricated with a considerably high energy input ($E_{\text{area}} = 11.1$ J/mm^2) because the overall sample was assumed to hold at a higher temperature that exceeds the temperature range for γ → ε transformation. To make a better use of the mechanisms identified in the presented study, a feasible control of phase constitution and distribution of γ/ε phases needs to be developed in PBF-EB of CCM alloy in the future, in which broader process conditions that affect the holding temperature and building period need to be considered such as preheating temperature, scan strategy, selective melting area, size and geometry of built object and the position within the object.

5. Conclusions

Through the experimental characterization and the analysis of the simulation results, the mechanisms of microstructural heterogeneity regarding isothermal γ → ε phase transformation in PBF-EB-built Co-Cr-Mo alloy were analyzed and can be summarized as follows:

1) The difference in γ/ε phase distribution was a result of the thermal history. The thermal history determined the method by which the γ → ε phase transformation is taking place.

2) In the sample with a lower energy input ($E_{\mathrm{area}} = 2.6$ J/mm^2), γ → ε martensitic transformation with S-N OR was dominant. With the building height increasing away from the base plate, ε phase fraction decreased, because the holding time for martensitic transformation decreased.
3) In the sample with a higher energy input ($E_{\mathrm{area}} = 4.4$ J/mm^2), the ε phase with near-random orientation formed via diffusional-massive transformation. ε phase presented only in a short range of the lower part away from the bottom where the period required for massive γ → ε transformation is relatively short.

Acknowledgments

This work was supported by Grants-in-Aid for Scientific Research (KAKENHI) (grant numbers 26289252, 15K14154, 17H01329 and 18H03834) from the Japan Society for the Promotion of Science (JSPS). This work was also partly supported by the Japan Ministry of Economy, Trade and Industry (METI); the New Energy and Industrial Technology Development Organization (NEDO); the Technology Research Association for Future Additive Manufacturing (TRAFAM); and the "Creation of Life Innovation Materials for Interdisciplinary and International Researcher Development" project.

References

[1] B. Almangour, Additive Manufacturing of Emerging Materials, Springer International Publishing, Cham, 2018.
[2] T. DebRoy, H.L. Wei, J.S. Zuback, T. Mukherjee, J.W. Elmer, J.O. Milewski, A.M. Beese, A. Wilson-Heid, A. De, W. Zhang, Progress in Materials Science 92 (2018) 112–224.
[3] C. Körner, International Materials Reviews 61 (2016) 361–377.
[4] L.E. Murr, Journal of Materials Science and Technology 32 (2016) 987–995.
[5] C. Petit, E. Maire, S. Meille, J. Adrien, S. Kurosu, A. Chiba, Materials Characterization 116 (2016) 48–54.
[6] Y. Koizumi, A. Okazaki, A. Chiba, T. Kato, A. Takezawa, Additive Manufacturing 12 (2016) 305–313.
[7] X. Tan, P. Wang, S. Nai, E. Liu, S.B. Tor, in: Proceedings of the International Conference on Progress in Additive Manufacturing, Pro-AM, 2018, pp. 535–540.

[8] X.P. Tan, P. Wang, Y. Kok, W.Q. Toh, Z. Sun, S.M.L. Nai, M. Descoins, D. Mangelinck, E. Liu, S.B. Tor, Scripta Materialia 143 (2018) 117–121.

[9] D.D. Xiang, P. Wang, X.P. Tan, S. Chandra, C. Wang, M.L.S. Nai, S.B. Tor, W.Q. Liu, E. Liu, Materials Science and Engineering: A 765 (2019) 138270.

[10] Y. Kok, X.P. Tan, P. Wang, M.L.S. Nai, N.H. Loh, E. Liu, S.B. Tor, Materials and Design 139 (2018) 565–586.

[11] W. Xu, M. Brandt, S. Sun, J. Elambasseril, Q. Liu, K. Latham, K. Xia, M. Qian, Acta Materialia 85 (2015) 74–84.

[12] X. Tan, Y. Kok, W.Q. Toh, Y.J. Tan, M. Descoins, D. Mangelinck, S.B. Tor, K.F. Leong, C.K. Chua, Scientific Reports 6 (2016) 26039.

[13] S.H. Sun, Y. Koizumi, S. Kurosu, Y.P. Li, A. Chiba, Acta Materialia 86 (2015) 305–318.

[14] D. Wei, Y. Koizumi, A. Chiba, K. Ueki, K. Ueda, T. Narushima, Y. Tsutsumi, T. Hanawa, Additive Manufacturing 24 (2018) 103–114.

[15] T. Takashima, Y. Koizumi, Y. Li, K. Yamanaka, T. Saito, A. Chiba, Materials Transactions 57 (2016) 2041–2047.

[16] K. Yamanaka, M. Mori, A. Chiba, Metallurgical and Materials Transactions A: Physical Metallurgy and Materials Science 43 (2012) 5243–5257.

[17] H.F. López, A.J. Saldivar-Garcia, Metallurgical and Materials Transactions A: Physical Metallurgy and Materials Science 39 (2008) 8–18.

[18] A.L. Ramirez-Ledesma, E. Lopez-Molina, H.F. Lopez, J.A. Juarez-Islas, Acta Materialia 111 (2016) 138–147.

[19] S. Kurosu, H. Matsumoto, A. Chiba, Metallurgical and Materials Transactions A: Physical Metallurgy and Materials Science 41 (2010) 2613–2625.

[20] C.B. Song, H.B. Park, H.G. Seong, H.F. López, Metallurgical and Materials Transactions A: Physical Metallurgy and Materials Science 37 (2006) 3197–3204.

[21] G. Barucca, E. Santecchia, G. Majni, E. Girardin, E. Bassoli, L. Denti, A. Gatto, L. Iuliano, T. Moskalewicz, P. Mengucci, Materials Science and Engineering C 48 (2015) 263–269.

[22] Y. Kajima, A. Takaichi, N. Kittikundecha, T. Nakamoto, T. Kimura, N. Nomura, A. Kawasaki, T. Hanawa, H. Takahashi, N. Wakabayashi, Materials Science and Engineering A 726 (2018) 21–31.

[23] K. Ren, Y. Chew, Y.F. Zhang, G.J. Bi, J.Y.H. Fuh, Journal of Materials Processing Technology 271 (2019) 178–188.

[24] P. Promoppatum, S.-C. Yao, P.C. Pistorius, A.D. Rollett, P.J. Coutts, F. Lia, R. Martukanitz, Progress in Additive Manufacturing 3 (2018) 15–32.

[25] W. Yan, Y. Lian, C. Yu, O.L. Kafka, Z. Liu, W.K. Liu, G.J. Wagner, Computer Methods in Applied Mechanics and Engineering 339 (2018) 184–204.

[26] W.K. Liu, Y.C. Shin, Computational Mechanics 61 (2018) 519–520.

[27] Y. Zhao, Y. Koizumi, K. Aoyagi, D. Wei, K. Yamanaka, A. Chiba, Materialia 6 (2019) 100346.

[28] *FLOW-3D*® Version 11.2 [Computer software]. (2017). Santa Fe, NM: Flow Science, Inc. https://www.flow3d.com.

[29] R.W. Messler, Principles of Welding, Wiley-VCH Verlag GmbH, Weinheim, Germany, 1999.

[30] Y. Zhao, Y. Koizumi, K. Aoyagi, D. Wei, K. Yamanaka, A. Chiba, Additive Manufacturing 26 (2019) 202–214.

[31] S. Loewy, B. Rheingans, S.R. Meka, E.J. Mittemeijer, Acta Materialia 64 (2014) 93–99.

[32] K. Aoyagi, H. Wang, H. Sudo, A. Chiba, Additive Manufacturing 27 (2019) 353–362.

[33] S. Cao, J.C. Zhao, Acta Materialia 88 (2015) 196–206.

[34] S. Mayer, M. Petersmann, F.D. Fischer, H. Clemens, T. Waitz, T. Antretter, Acta Materialia 115 (2016) 242–249.

[35] J.W. Christian, H.M. Otte, Physics Today 19 (1966) 78–81.

[36] The Japan Institute of Metals and Materials, Thermodynamics of Microstructure, 1st ed., The Japan Institute of Metals and Materials, Sendai, 2005.

[37] S.S. Naghavi, V.I. Hegde, C. Wolverton, Acta Materialia 132 (2017) 467–478.

[38] J.O. Andersson, T. Helander, L. Höglund, P. Shi, B. Sundman, Calphad: Computer Coupling of Phase Diagrams and Thermochemistry 26 (2002) 273–312.

[39] The Japan Institute of Metals and Materials, Thermal Dynamics of Microstructure, Maruzen, Tokyo, 2005.

[40] Z. Nishiyama, Martensitic Transformation, ACADEMIC PRESS, New York, 1978.

[41] G.B. Olson, M. Cohen, Metallurgical Transactions A 7 (1976) 1897–1904.

[42] S. Kajiwara, Materials Transactions 33 (1992) 1027–1034.

[43] C.H. Shih, B.L. Averbach, M. Cohen, JOM 7 (1955) 183–187.

Figure and table captions

Table 1 Chemical composition of gas-atomized Co-28Cr-6Mo alloy powder

Fig. 1. (a) The samples with cube-shape and dimensions of 10 mm ×10 mm ×10 mm were built on a base plate with the size of 150 mm × 150 mm × 10 mm and (b) process parameters of each sample is shown in the corresponding position.

Fig. 2. Schematic diagram of the modeling simplification for numerical simulation of thermal history: (a) the moving-spot heat source was approximated as an equivalent plane heat source; (b) the layer-by-layer building was simplified as bulk-increment.

Fig. 3. (a) EBSD phase map of vertical cross-sectional microstructure and (b)(c) EBSD pole figures of selected ε grain and original γ grain at the lower part of the as-PBF-EB-built sample. The process parameter is P= 600 W, V= 300 mm/s, l_{off}= 455 μm.

Fig. 4. Selected samples that exhibited typical microstructure locates at (a) axisymmetric positions with respect to the base plate. The field-of-view is depicted in (b). (c)(d) EBSD IPF maps and phase maps of vertical cross-sectional microstructure in different parts along the building height. The process parameters are: P= 100 W, V= 300 mm/s, l_{off}= 125 μm (Sample A); P= 1000 W, V= 300 mm/s, l_{off}= 750 μm (Sample B).

Fig. 5. Experimental thermal history during the PBF-EB process at the bottom center of the base plate measured by a thermo-couple equipped in the building chamber.

Fig. 6. Top view of the simulated temperature field of the base plate. The base plate was heated by an equivalent plane heat source until the temperature in the bottom center reached 1098 K.

Fig. 7. Simulated temperature fields of (a) Sample A and (b) Sample B during the building process. (c)(d) The evolution of temperature at the center position in each increment of (c) Sample A and (d) Sample B.

Fig. 8. Isothermal TTT curve of the γ → ε diffusional-massive transformation. The red and green curves present the start and end of the transformation, respectively. The building period of PBF-EB was additionally annotated. The temperature ranges that Sample A and Sample B underwent during PBF-EB are annotated on the right side.

Fig. 9. EBSD pole figures taken from the γ and ε phases in the middle and lower parts of (a) Sample A and (b) Sample B.

Fig. 10. Histograms of misorientation angle between adjacent ε phase in (a) Sample A and (b) Sample B.

Fig. 11. EBSD IPF maps and phase maps of vertical cross-sectional microstructure in the sample almost without the ε phase. The process parameter is P= 1000 W, V= 100 mm/s, l_{off}= 900 μm.

Table list:

Table 1 Chemical composition of gas-atomized Co-28Cr-6Mo alloy powder.

Composition	Cr	Mo	Ni	Fe	Si	Mn	C	N	Co
Value (mass%)	27.7	6.1	0.02	0.05	0.57	0.6	0.05	0.1	Bal.

Figure list:

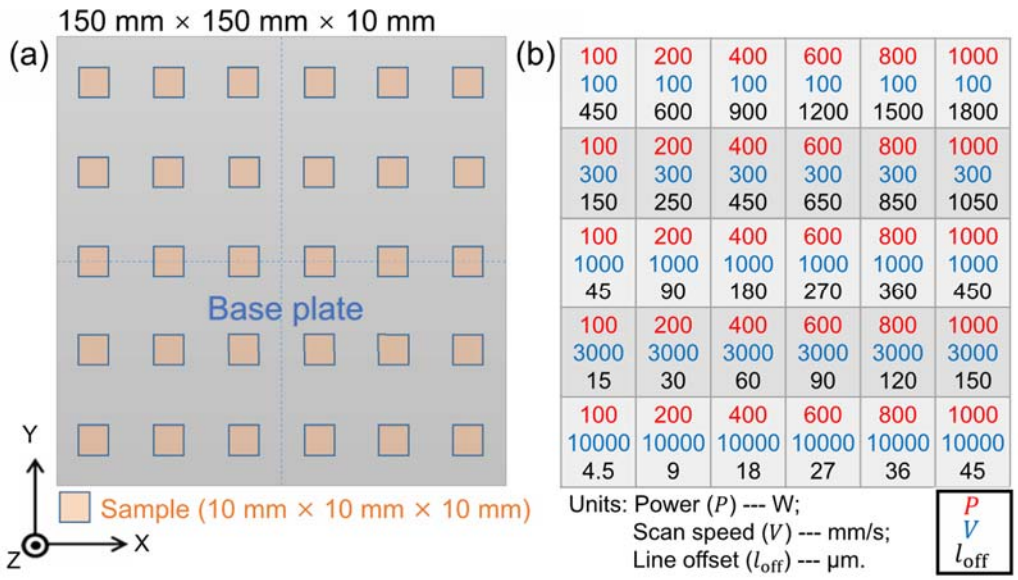

Fig. 1. (a) The samples with cube-shape and dimensions of 10 mm ×10 mm ×10 mm were built on a base plate with the size of 150 mm × 150 mm × 10 mm and (b) process parameters of each sample is shown in the corresponding position.

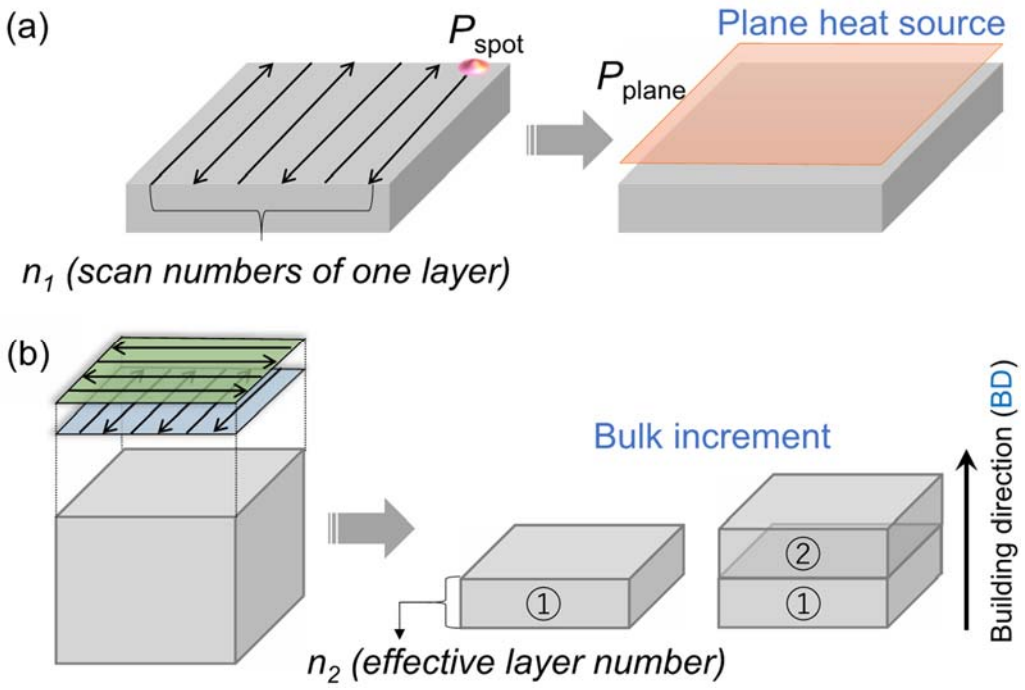

Fig. 2. Schematic diagram of the modeling simplification for numerical simulation of thermal history: (a) the moving-spot heat source was approximated as an equivalent plane heat source; (b) the layer-by-layer building was simplified as bulk-increment.

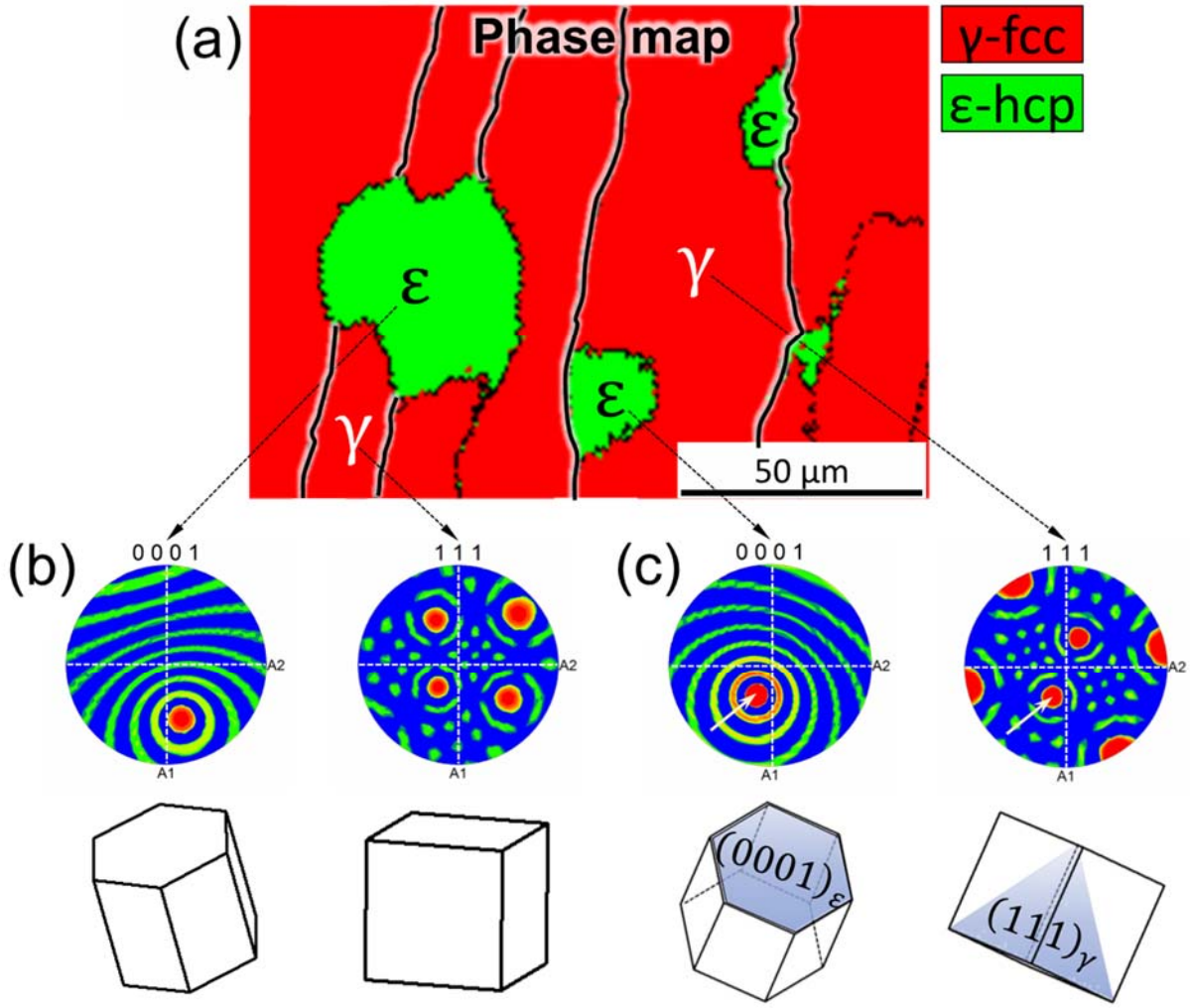

Fig. 3. (a) EBSD phase map of vertical cross-sectional microstructure and (b)(c) EBSD pole figures of selected ε grain and original γ grain at the lower part of the as-PBF-EB-built sample. The process parameter is P= 600 W, V= 300 mm/s, l_{off}= 455 μm.

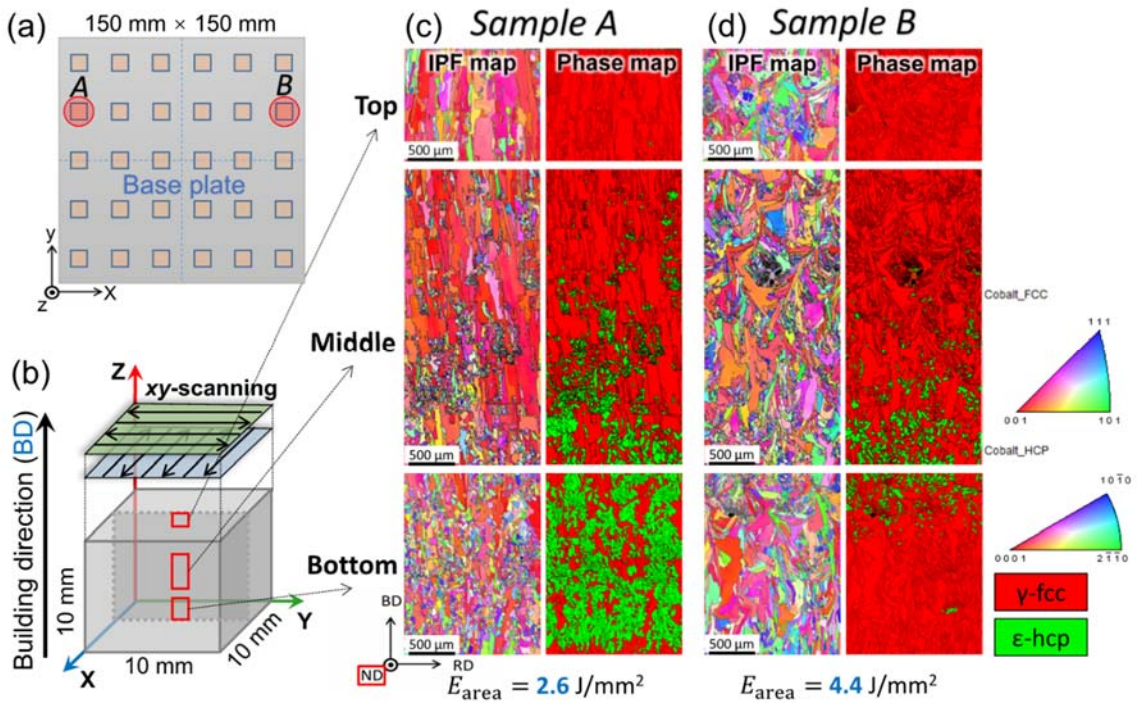

Fig. 4. Selected samples that exhibited typical microstructure locates at (a) axisymmetric positions with respect to the base plate. The field-of-view is depicted in (b). (c)(d) EBSD IPF maps and phase maps of vertical cross-sectional microstructure in different parts along the building height. The process parameters are: P= 100 W, V= 300 mm/s, l_{off}= 125 µm (Sample A); P= 1000 W, V= 300 mm/s, l_{off}= 750 µm (Sample B).

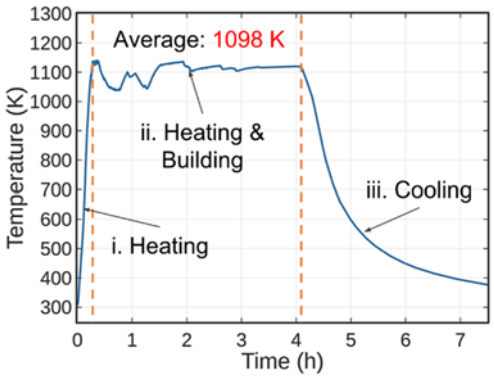

Fig. 5. Experimental thermal history during the PBF-EB process at the bottom center of the base plate measured by a thermo-couple equipped in the building chamber.

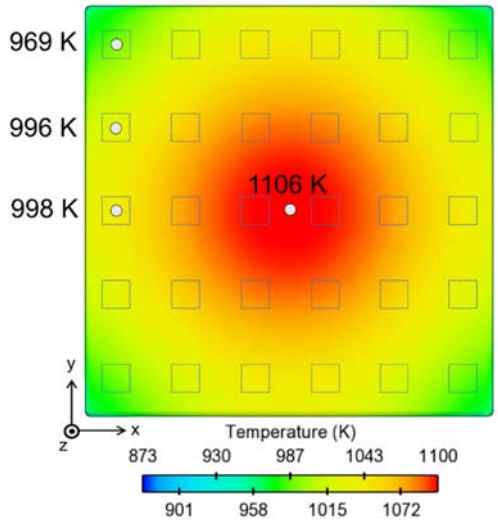

Fig. 6. Top view of the simulated temperature field of the base plate. The base plate was heated by an equivalent plane heat source until the temperature in the bottom center reached 1098 K.

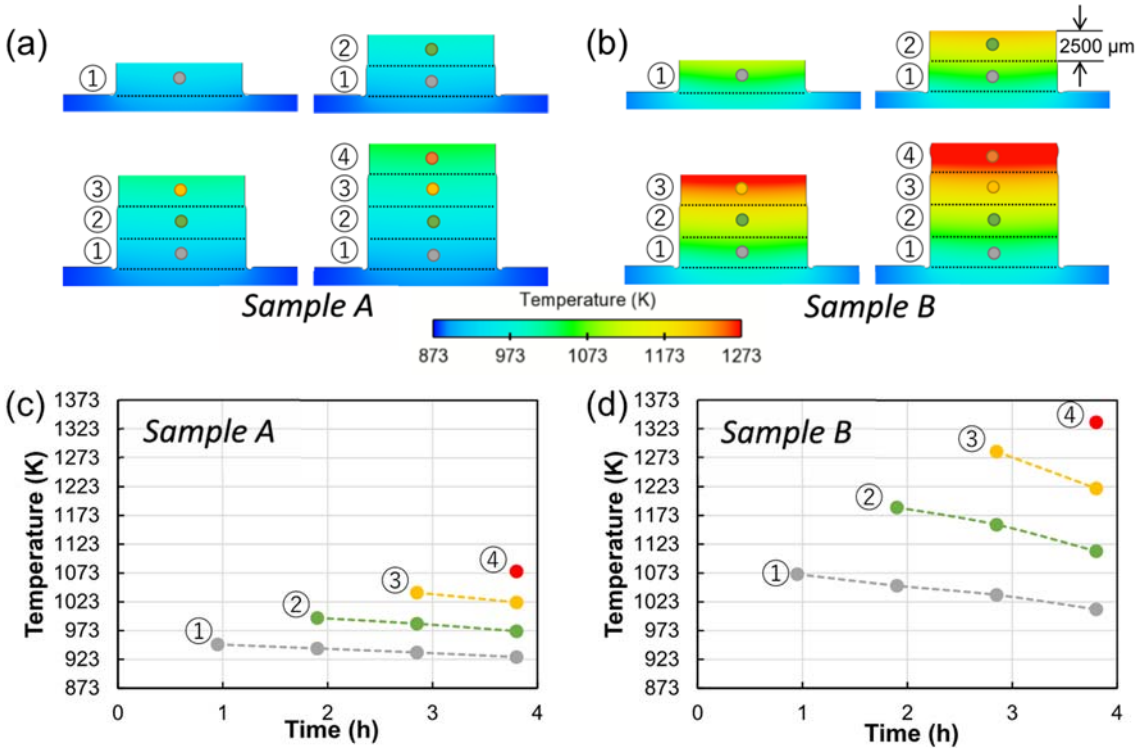

Fig. 7. Simulated temperature fields of (a) Sample A and (b) Sample B during the building process. (c)(d) The evolution of temperature at the center position in each increment of (c) Sample A and (d) Sample B.

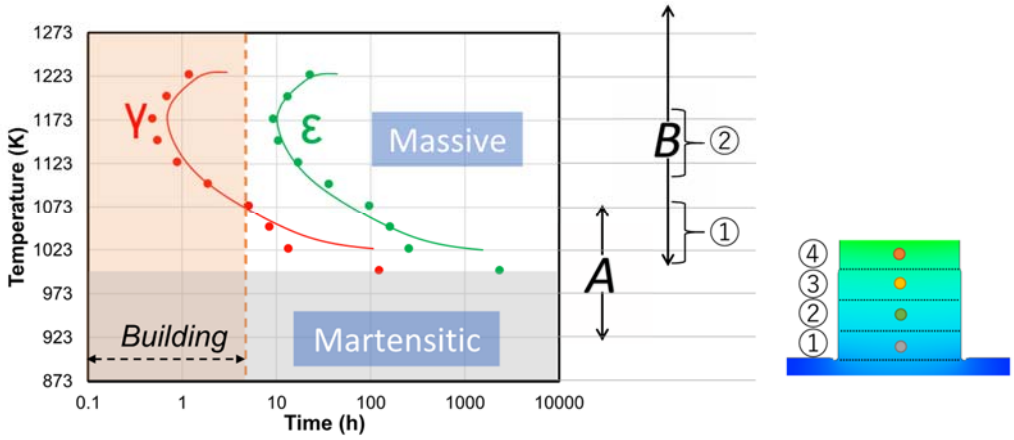

Fig. 8. Isothermal TTT curve of the γ → ε diffusional-massive transformation. The red and green curves present the start and end of the transformation, respectively. The building period of PBF-EB was additionally annotated. The temperature ranges that Sample A and Sample B underwent during PBF-EB are annotated on the right side.

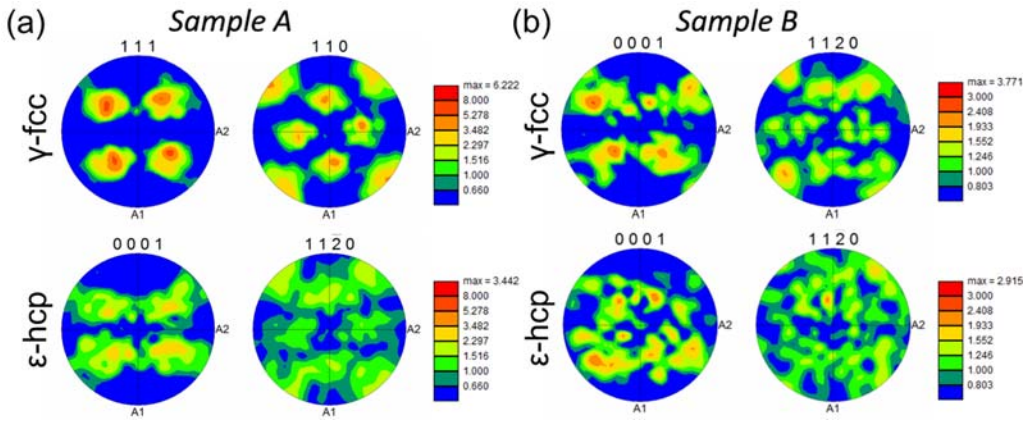

Fig. 9. EBSD pole figures taken from the γ and ε phases in the middle and lower parts of (a) Sample A and (b) Sample B.

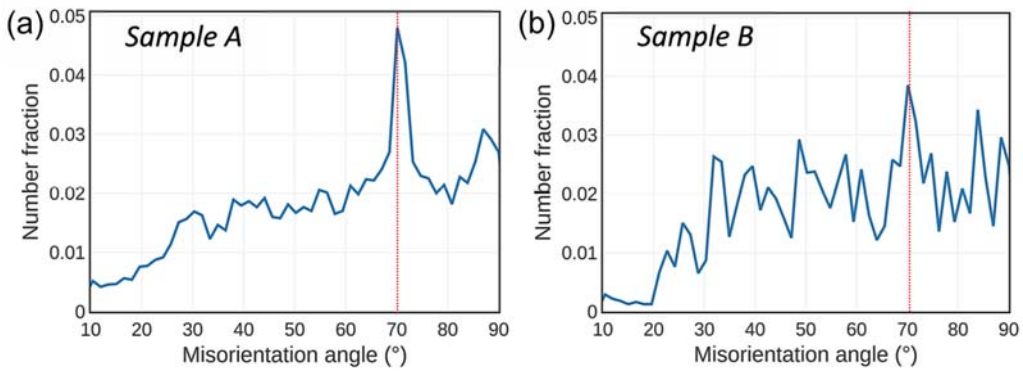

Fig. 10. Histograms of misorientation angle between adjacent ε phase in (a) Sample A and (b) Sample B.

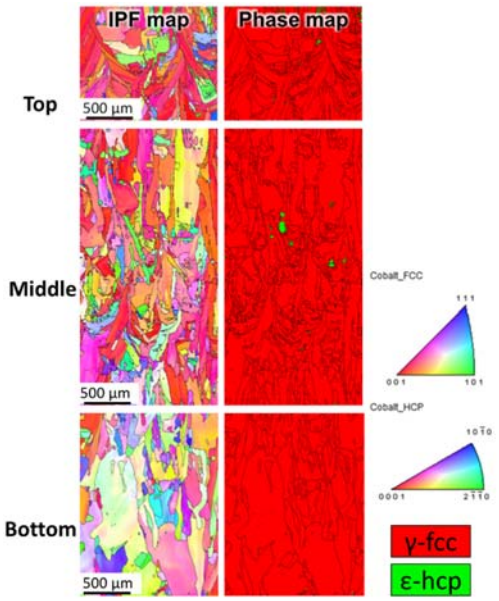

Fig. 11. EBSD IPF maps and phase maps of vertical cross-sectional microstructure in the sample almost without the ε phase. The process parameter is P= 1000 W, V= 100 mm/s, l_{off}= 900 μm.

Highlights

- The microstructural heterogeneity of PBF-EB-built CoCrMo alloy was analyzed
- The isothermal γ→ε transformation occurred during the PBF-EB fabrication
- The difference in γ/ε phase distribution was a result of the thermal history
- Manipulating energy input can control isothermal γ→ε transformation behaviors